Bulletin of the Seismological Society of America, Vol. 100, No. 5A, pp. 2250–2263, October 2010, doi: 10.1785/0120090319

Phase Velocity Variation at Periods of 0.5–3 Seconds in the Taipei Basin of Taiwan from Correlation of Ambient Seismic Noise

by Yu-Chih Huang, Huajian Yao, Bor-Shouh Huang, Robert D. van der Hilst,
Kuo-Liang Wen, Win-Gee Huang, and Chi-Hsuan Chen

Abstract Improving seismic hazard mitigation of the densely populated metropolitan area of and around the capital of Taiwan requires detailed knowledge of the 3D crustal structure of Taipei basin. The high levels of ambient noise and the low levels of regional seismicity of this region complicate investigations of crustal structure with traditional seismic exploration or earthquake tomography methods. We investigate the shallow crust in the metropolitan region using surface wave array tomography with time domain empirical Green's function (TDEGF) inferred from correlation of ambient seismic noise. Analysis of the TDEGF amplitudes suggests that the dominant sources of ambient seismic noise are the coastlines and shallow continental shelf of the Taiwan Strait, northwest of the study region. Our study demonstrates that ambient seismic noise tomography is feasible at periods of 0.5–3 s, which is much shorter than the 10–30 s used in most other studies, and which opens new opportunities for high resolution studies of near-surface heterogeneity. The lateral variation in Rayleigh wave phase velocity correlates well with surface geology and suggests that faults play an important role in the regional tectonic setting. High phase velocities mark the Tatun volcanic area, the Kuanyin Mountain dominated by Quaternary igneous rock, and the Miocene Western Foothills south of the Taipei fault. Low phase velocities characterize regions are along western and southeastern edges of the Taipei basin and the Pleistocene Linkou tableland. Main faults in the region are either marked by low phase velocities or define transitions between regions of high- and low-velocity anomalies.

Introduction

Regional Geology

Located near the northern tip of the Island of Taiwan (Fig. 1), Taipei basin is home to the Taipei metropolitan area, which includes Taipei City (the capital of Taiwan) and Taipei County. The nearly triangular basin (~20 km across) is surrounded by the Quaternary Tatun volcanic area in the north, the Pleistocene Linkou tableland and Quaternary volcanic Kuanyin Mountain in the west, and the Tertiary Western Foothills in the south and east. Quaternary Tatun and Kuanyin volcanoes erupted and covered older Tertiary Western Foothills and Pleistocene Linkou tableland strata (Teng *et al.*, 2001). The detailed surface geology is shown in Figure 2.

According to widely distributed drilling wells by the Central Geological Survey (CGS) in the Taipei basin, the basement of the Taipei basin is the deformed Tertiary strata and is filled with flat-lying Holocene sediments (Teng *et al.*, 2001). Wang *et al.* (2004) combined over 30 drilling wells and 300 shallow reflection seismic lines to investigate subsurface velocity structure up to about 500 m depth. Their result shows that this Tertiary basement is in a half-graben shape, and the deepest part is along the western border of the Taipei basin, where the Chinshan fault and the Shanchiao fault are located (Fig. 1). Based on CGS (2000), there are two active faults and two suspected active faults in the Taipei basin. Shanchiao fault is a normal fault with high angle dipping to the east, where the Taipei basin is on the hanging wall and the Linkou tableland is on the footwall. Chinshan fault is a thrust fault just to the west of the Shanchiao fault; it cuts across the Tatun volcanic area. Kanchiao fault and Taipei fault are two suspected active faults and are also known as important geologic structures in the Taipei basin.

Previous Studies in the Taipei Basin

Because serious damage caused by earthquakes is usually due to the amplification of seismic energy in alluvial deposits (Wen and Peng, 1998), studies of drilling wells, seismic reflection profiles, and other measurements available for the Taipei basin have in the past decade focused primarily on the geologic and seismic structure of the sediment layer in the top several hundred meters. To simulate strong ground motion better, it is also important to know the shallow crust velocity structure, but traditional methods for determining

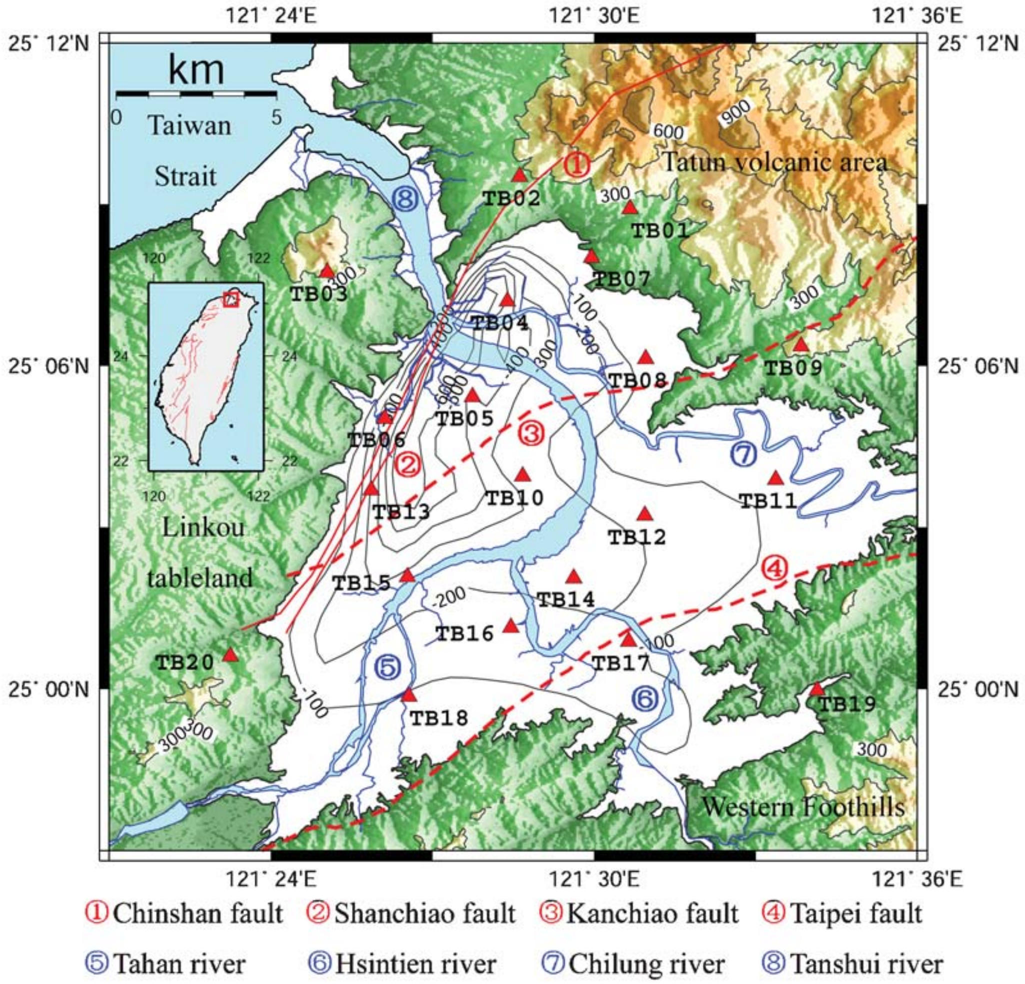

Figure 1 Topography, Tertiary basement, geologic structure, faults, river systems, and station locations in the Taipei basin. The topography map is drawn with 300 m interval contour based on 40 m Digital Terrain Model (DTM). The depth of the Tertiary basement is drawn with 100 m interval contour (from Wang *et al.*, 2004). There are two active faults shown as the red solid lines and two suspected active faults shown as the red dash lines. Station locations are shown as red triangles with station names underneath. The inset figure shows the locations of the study region (red box) and the active faults (red lines) on the island of Taiwan.

crustal heterogeneity, such as active source experiments and passive seismic monitoring, are not well suited to study the shallow structure in the Taipei basin. This has two main reasons. On the one hand, the urban character and high seismic noise levels of the densely populated metropolitan area prohibit comprehensive active source experiments. On the other hand, the (fortunately) low level of seismicity does not provide enough (natural) sources for high-resolution imaging and tomography. In absence of internally consistent models for the 3D structure of Taipei basin, ground-motion simulations (e.g., Lee *et al.*, 2008) often combine high-resolution local models, for instance the Quaternary sediment model due to Wang *et al.* (2004), with larger scale regional models, such as the model of Kim *et al.* (2005).

Using fundamental mode Love waves ($T = 2$–7 s) excited by the 1994 Nanao earthquake and recorded by the Taiwan Strong Motion Instrumentation Program (TSMIP), Chung and Shin (1999) obtained lateral variation of shear velocity at 1–4 km depth in the shallow crust of the Taipei basin. Unfortunately, not all TSMIP stations were equipped with a GPS timing system at that time, and poorly known timing errors induced uncertainty in these wave speed estimates.

Ambient Seismic Noise Studies

Here we present results of passive-source surface wave array tomography of the crust of Taipei basin. The time domain empirical Green's function (TDEGF) can be estimated from the correlation of diffuse wave fields, such as seismic coda waves or ambient seismic noise, and is now routinely used to investigate the subsurface shear-wave velocity structure. Campillo and Paul (2003) and Sabra *et al.* (2005a) confirmed that the particle motion in the cross correlation of vertical component data is dominated by Rayleigh-wave propagation. Furthermore, Shapiro and Campillo (2004) and Shapiro *et al.* (2005) compared TDEGFs and dispersion curves obtained from ambient seismic noise with direct surface waves of seismic events and proved their consistency.

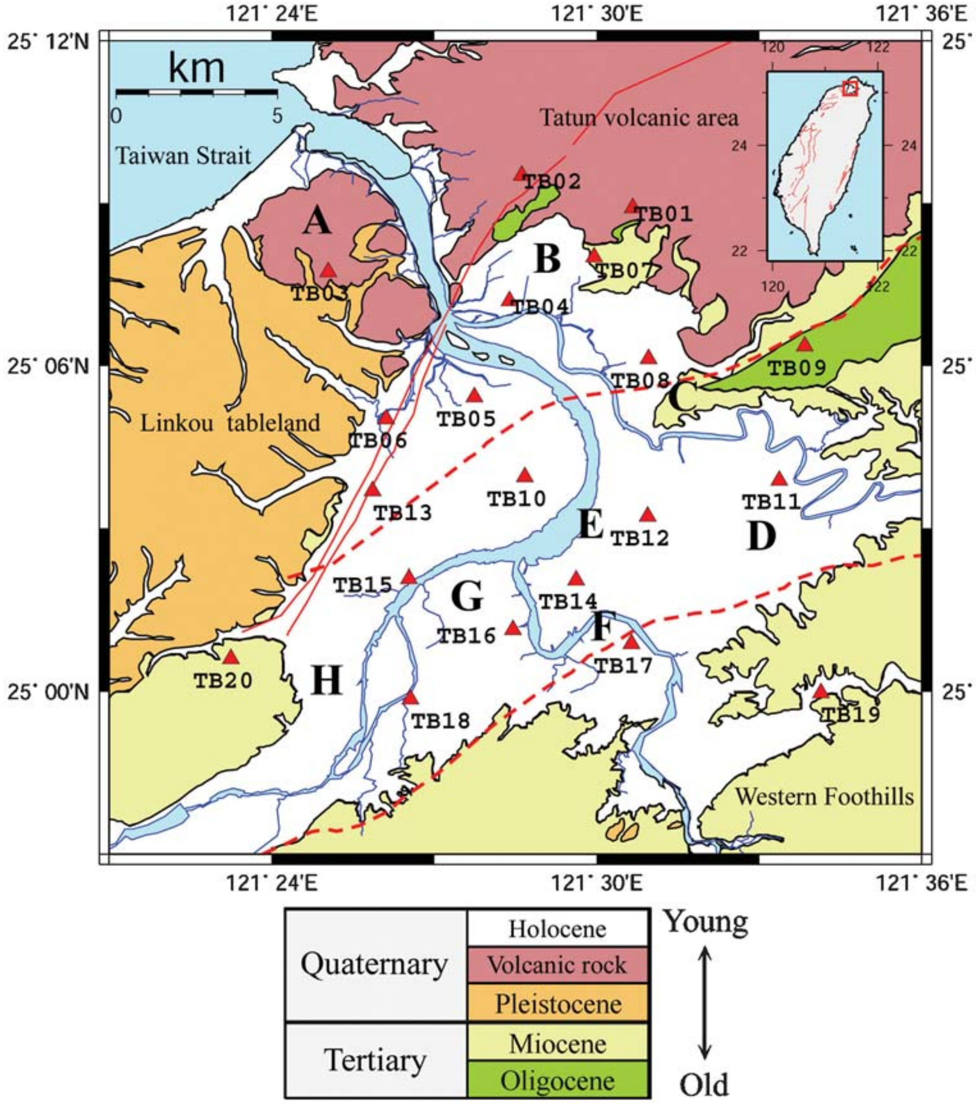

Figure 2. Surface geology with faults, river systems, and station locations in the Taipei basin. The abbreviations are A: Kuanyin Mountain, B: Kuantu Plain, C: Yuanshan, D: Sungshan, E: Wanhua, F: Yunghe, G: Panchiao, and H: Shulin. The inset figure is the same as Figure 1.

Yao *et al.* (2009) also demonstrated the agreement between the Rayleigh phase velocity dispersion measured from vertical component TDEGFs and earthquake Rayleigh-wave data in southeast Tibet. These studies confirm that the correlation between vertical component data (seismic coda wave or ambient seismic noise) relates to Rayleigh-wave propagation between two stations.

This method does not require earthquakes, but uses structural signals contained in continuously recorded ambient seismic noise. Yao *et al.* (2006) showed that stable results can be obtained from relatively short periods of (recording) time. The depth range that can be studied depends on the frequency band of the TDEGFs (which, in turn, are limited by the aperture of the receiver array), and lateral resolution depends on the coverage and density of interstation paths. Over the past five years, ambient seismic noise tomography has provided important constraints on 3D crustal structure in many regions in the world, including the western United States (Sabra *et al.*, 2005a; Sabra *et al.*, 2005b; Shapiro *et al.*, 2005; Gerstoft and Sabra *et al.*, 2006; Lin *et al.*, 2008; Bensen *et al.*,

Table 1
Statistics of Station-Pair Distance in This Research in the Taipei Basin

Station-Pair Distance (km)	0–5 km	5–10 km	10–15 km	15–20 km	20–25 km
Station-pair number	30	78	60	20	2
Percentage (%)	15.79	41.05	31.58	10.53	1.05

2008), southeastern Tibet (Yao *et al.*, 2006, 2008), Korea (Kang and Shin, 2006), New Zealand (Lin *et al.*, 2007), and Europe (Yang *et al.*, 2007). The lateral extent of most of these studies ranges from several hundred to several thousand kilometers, with interstation distances of at least several dozens of kilometers. The period range of the data used is mostly in the range of 10–30 s, with most noise produced by ocean waves interacting with the seafloor or coastlines (e.g., Stehly *et al.*, 2006; Yang and Ritzwoller, 2008).

Outline of This Study

The main objective of this study is to investigate crustal structure of the Taipei basin (20×20 km^2) using ambient seismic noise tomography and data from a receiver array with about 5 km station spacing. Three months of vertical component data (from mid-July to mid-October 2005) were selected to produce TDEGFs from one-bit noise cross-correlation (Data and Processing section). We then measure phase velocity dispersion curves in the period band 0.5–5 s from the retrieved TDEGFs; with these dispersion measurements we construct 2D phase velocity maps at different periods (Dispersion Analysis and Phase Velocity Maps section). Finally, we discuss the directionality of ambient seismic noise recorded in the Taipei basin as well as the geologic implications of the 2D phase velocity maps (Discussion section).

Data and Processing

Data and TDEGF

In order to monitor microearthquakes and understand potential seismic sources in the Taipei basin, the Institute of Earth Sciences, Academia Sinica deployed 20 broadband seismograph stations in mid-2005 in the basin area (Figs. 1 and 2). There are a total of 190 station pairs, among which 138 station pairs (72.63%) are in a distance range between 5 and 15 km (Table 1). Each station is equipped with a KS-2000 broadband sensor (0.02–120 s), DL24 digitizer (24 bits), and GPS timing system. Most stations functioned well after one month deployment; therefore, this research selected three months data, from mid-July to mid-October in 2005, for ambient seismic noise analysis. For data quality control, we checked the timing accuracy of the BHZ channel (vertical component, 20 Hz sampling rate) for all stations by comparing signals from some large seismic events with each other. We eliminated data when we suspected timing problems or when we observed spurious signals.

We used a one-bit cross-correlation method (OBCC) (e.g., Larose *et al.*, 2004; Shapiro and Campillo, 2004) to obtain the vertical component time domain cross-correlation function $C_{AB}(t)$ for station pairs A and B. The OBCC enhances the amplitude of ambient seismic noise relative to that from large seismic events. Yao *et al.* (2006) showed that the recovered TDEGFs from OBCC are almost identical, with or without signals from large earthquakes. Therefore, in this study we simply use continuous recordings without removing earthquake signals. OBCC enhances the signal-to-noise ratio (SNR) of $C_{AB}(t)$ compared to cross-correlation of full waveform data.

The TDEGF is derived from the time-derivative of $C_{AB}(t)$,

$$\frac{dC_{AB}(t)}{dt} = -\hat{G}_{AB}(t) + \hat{G}_{BA}(-t) \approx -G_{AB}(t) + G_{BA}(-t), \qquad (1)$$

where $\hat{G}(t)$ is the TDEGF and $G(t)$ is real time domain Green's function (Yao *et al.*, 2006; Yao and van der Hilst, 2009). $\hat{G}_{AB}(t)$ represents the TDEGF recorded at station B for a fictitious source at station A. Vice versa, $\hat{G}_{BA}(t)$ is the

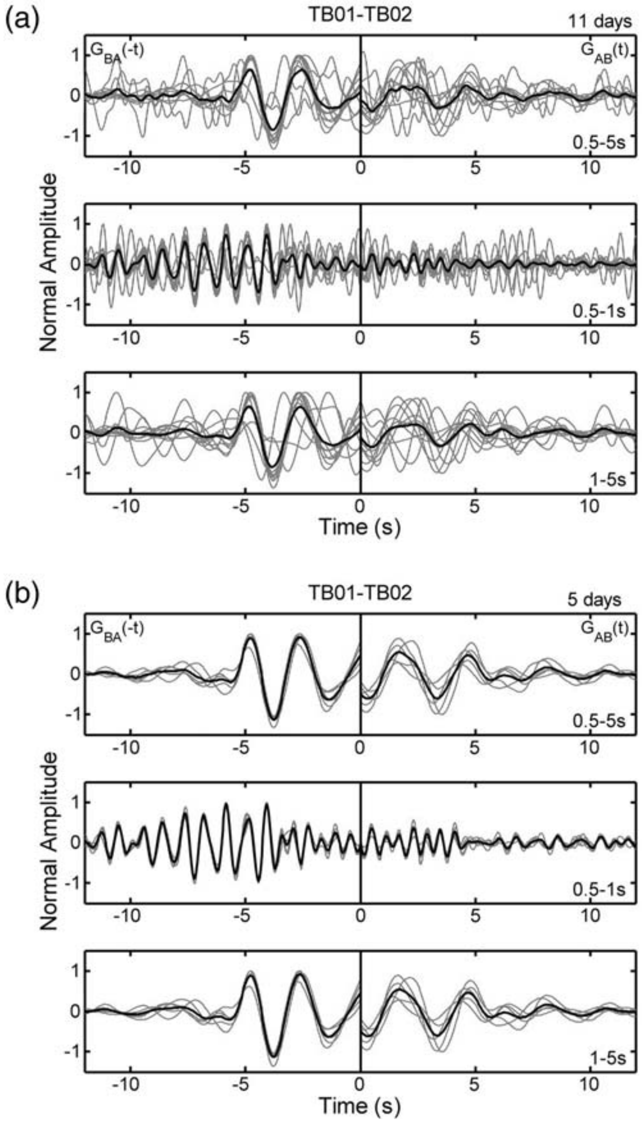

Figure 3. TDEGFs of station pair TB01–TB02 (a) with typhoon days, and (b) without typhoon days. TDEGFs are band-pass-filtered in three period bands: 0.5–5 s, 0.5–1 s, and 1–5 s. Gray lines show TDEGFs from daily data and the black lines show the stacked TDEGF of all daily TDEGFs. TDEGFs without typhoon days are more stable than with typhoon days, even for the shortest period band at 0.5–1 s.

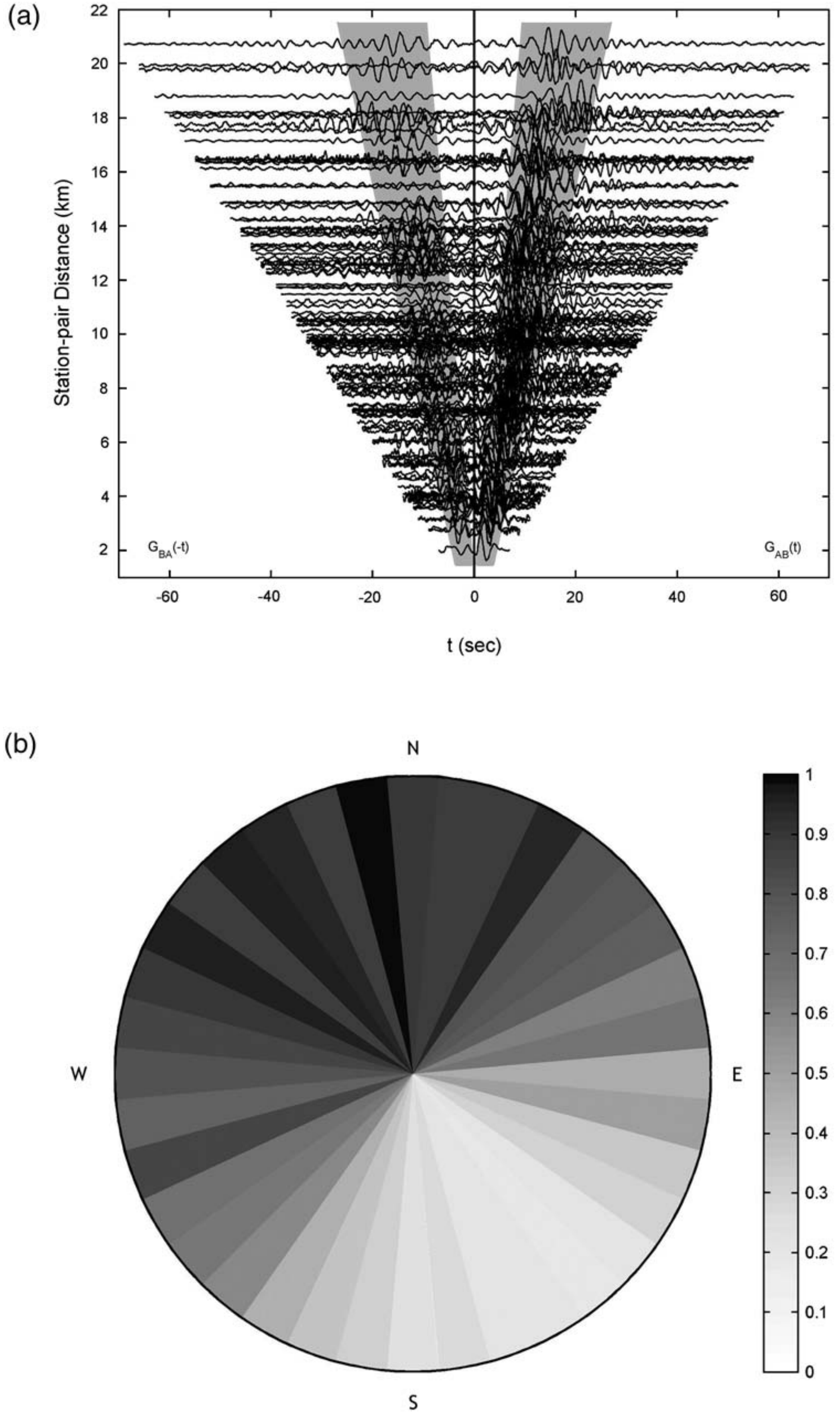

Figure 4. (a) All TDEGFs in the period band 0.5–5 s with SNR higher than 10. The gray area is defined as the main signal window with velocity 0.9–1.5 km/s. Noise window is defined as velocity 0.3–0.7 km/s. (b) Azimuthal dependence of the normalized amplitudes of TDEGFs. From (b), we see that ambient seismic noise sources are mainly coming from the northwest direction.

TDEGF at A for a fictitious source at B. Because we applied OBCC to vertical component ambient seismic noise data, the obtained TDEGFs relate to interstation Rayleigh-wave propagation (e.g., Shapiro and Campillo, 2004; Sabra *et al.*, 2005a; Shapiro *et al.*, 2005).

Effect of TDEGFs from Typhoons

Every year Taiwan is hit by several violent typhoons. In the summer of 2005, there were three violent typhoons passing across the island; others passed just near the coast. TDEGFs can be affected by transient sources. Figure 3 shows the

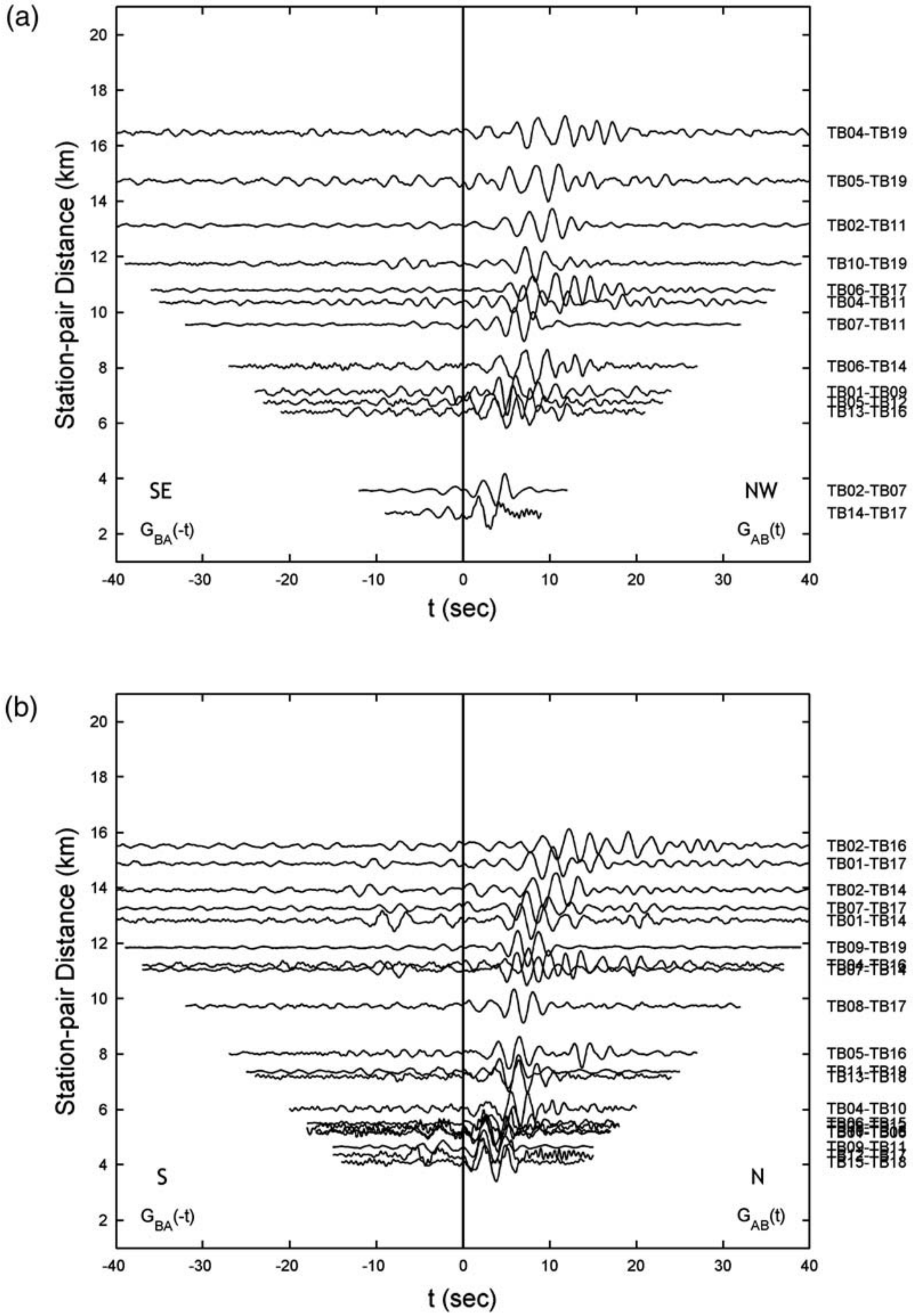

Figure 5. TDEGFs in the period band 0.5–5 s with SNR higher than 10 in 4 orientations of (a) northwest-southeast, (b) north–south, (c) northeast-southwest, and (d) east–west. Station locations and names are shown in Figures 1 and 2. (*Continued*)

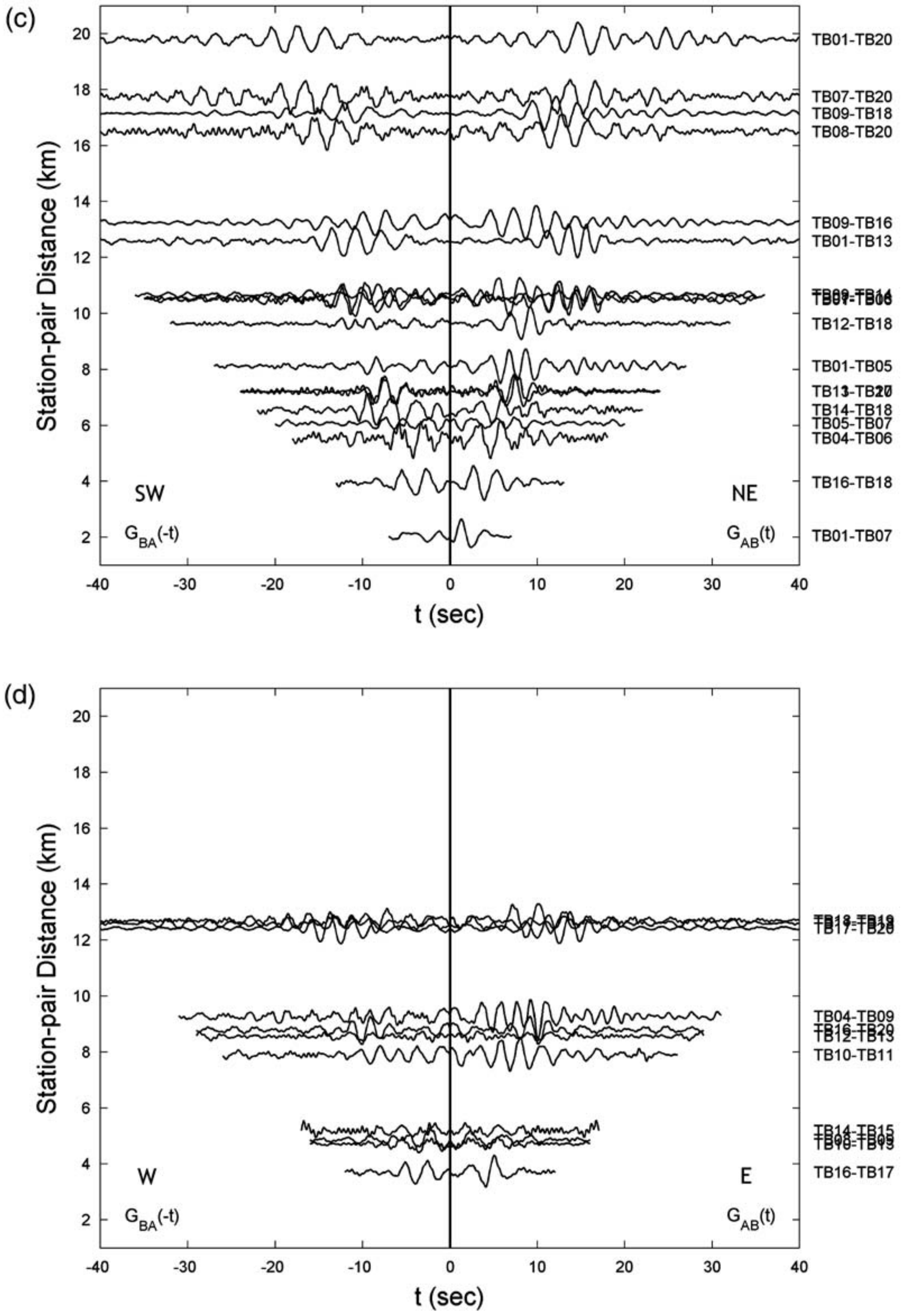

Figure 5. Continued.

difference of daily TDEGFs for the station pair TB01–TB02 from days with and without typhoons. TDEGFs without typhoon days (Fig. 3b) are more coherent and stable than with typhoon days (Fig. 3a), even in the 0.5–1 s period band. In order to minimize the influence of typhoons on TDEGFs, we excluded the time window from one day before to one day after the typhoon warnings. In total, we excluded data for 39 days; 49 days were kept for this ambient seismic noise study.

For each selected time window, we removed the mean and the trend and we band-pass-filtered the data (and the TDEGFs) between 0.5 and 5 s. Finally, for each station pair, we first calculated daily TDEGFs from OBCC of the selected

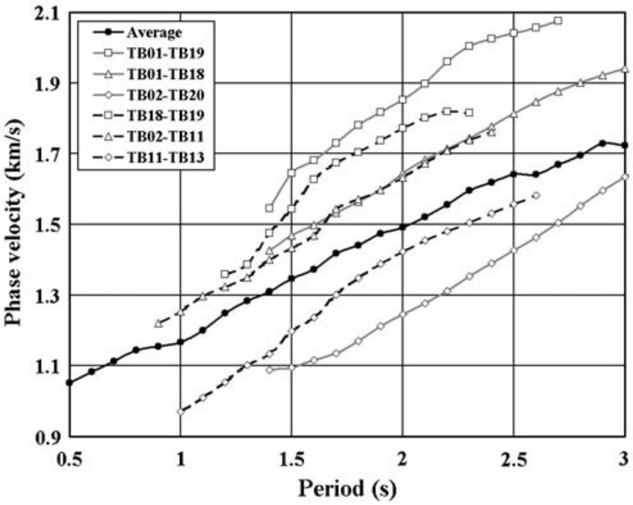

Figure 6. Phase velocity dispersion curves of some station pairs in the Taipei basin. The black solid line is the average phase velocity dispersion curve of all station pairs. The gray solid lines and black dashed lines are phase dispersion curves for some station pairs in the north–south and east–west direction, respectively. Station locations are shown in Figures 1 and 2.

daily recordings and then stacked all daily TDEGFs to obtain the averaged TDEGF. Figure 4a shows TDEGFs with SNR higher than 10, with clear surface wave propagation at an average wave speed of 1.2 km/s. The main signal is defined as the waveform within the velocity window 0.9–1.5 km/s and noise in the velocity window 0.3–0.7 km/s. The number of TDEGFs plotted is 124, which is about 65% of the total number of station pairs.

Directionality of TDEGFs

In theory, for an isotropic distribution of noise sources we expect $\hat{G}_{AB}(t)$ and $\hat{G}_{BA}(-t)$ to be time-symmetrical (e.g., Roux *et al.*, 2005). However, in practice, $\hat{G}_{AB}(t)$ and $\hat{G}_{BA}(-t)$ are usually asymmetrical due to uneven distribution of noise sources (e.g., Sabra *et al.*, 2005b; Yao *et al.*, 2006; Gerstoft and Sabra *et al.*, 2006; Shapiro *et al.*, 2006; Stehly *et al.*, 2006; Lin *et al.*, 2007; Yao *et al.*, 2009). Figure 5 displays the TDEGFs for station pairs in four orientations. Apparently, there is a clear difference between the first two (northwest-southeast and north–south) and the last two orientations (northeast-southwest and east–west). TDEGFs are asymmetric for station pairs in nearly northwest-southeast and north–south orientations (Fig. 5a,b), and the amplitude of $\hat{G}_{AB}(t)$ is much larger than that of $\hat{G}_{BA}(-t)$. This suggests that ambient seismic noise sources are much stronger from the northwest and north directions than from the southeast and south directions. TDEGFs are nearly symmetrical for station pairs in nearly northeast-southwest and east–west orientations (Fig. 5c,d), suggesting similar ambient seismic noise energy propagation through the array from northeast and southwest or east and west. Following Stehly *et al.* (2006), we determine the directions of background energy flow into the array with statistics of symmetry or asymmetry of TDEGFs, according to the orientations of station pairs. We kept only 124 TDEGFs (or 248 azimuths) from Figure 4a and separated the azimuths into 36 sectors (each sector is 10°). This method can only constrain the direction to, but not the location of, the sources of ambient seismic noise. Figure 4b shows the azimuthal dependence of the normalized amplitudes of TDEGFs, which confirms that ambient seismic noise sources at a very short period band (0.5–5 s) are mostly from the northwestern direction, that is, from the coastlines and continental shelf of the Taiwan Strait rather than the deep bathymetry of the Pacific Ocean.

Dispersion Analysis and Phase Velocity Maps

Phase Velocity Dispersion Curves from TDEGFs

As we have seen from Figures 4 and 5, the TDEGFs are sometimes not time-symmetrical. Previous studies (e.g., Lin *et al.*, 2007; Yang *et al.*, 2007; Yao *et al.*, 2008) suggested to stack the causal (positive-time) and acausal (negative-time) parts of TDEGF to enhance the symmetric component TDEGF, and thus suppress the effect of uneven distribution of ambient seismic noise sources. We followed this procedure and measured phase velocity dispersion curves within 0.5–5 s period band from the symmetric component TDEGFs using the phase image analysis method by Yao *et al.* (2006). Their method used far-field representation of surface wave propagation (e.g., Dahlen and Tromp, 1998) and an image transformation technique (Yao *et al.*, 2005) to determine phase velocities from peak points of TDEGF at corresponding periods. To ensure that the fundamental mode of the surface wave is sufficiently well developed to allow unambiguous dispersion measurement, we require that the interstation distance is at least three wavelengths. Consequently, the maximum period at which we can measure dispersion is determined by the interstation distance (Δ_{AB}) and the average phase velocity (v_{AB}):

$$\Delta_{AB} \geq 3\lambda = 3v_{AB} \cdot T, \quad (2)$$

where λ is the wavelength of surface waves at period T (Yao *et al.*, 2006).

The variation in elevation across the study region is small (less than 300 m, Fig. 1). Because the associated bias (less than 1%) is much smaller than the inferred variations in phase velocity, we ignore the effects of topography. Figure 6 shows phase velocity dispersion curves in the period band 0.5–3 s for some station pairs. For station pairs along the north–south direction, phase velocities are lower in the western edge (TB02–TB20) and higher in the eastern part (TB01–TB19) of the Taipei basin. The difference of phase velocities can reach around 600 m/s, while the average phase velocities are about 1.1–1.7 km/s in this period band. Along the east–west direction, phase velocities are lower in the central part (TB11–TB13) and higher in the northern (TB02–TB11) and southern (TB18–TB19) edge of the Taipei basin. The difference of phase velocities reaches around 350 m/s, which is smaller than that along the north–south direction.

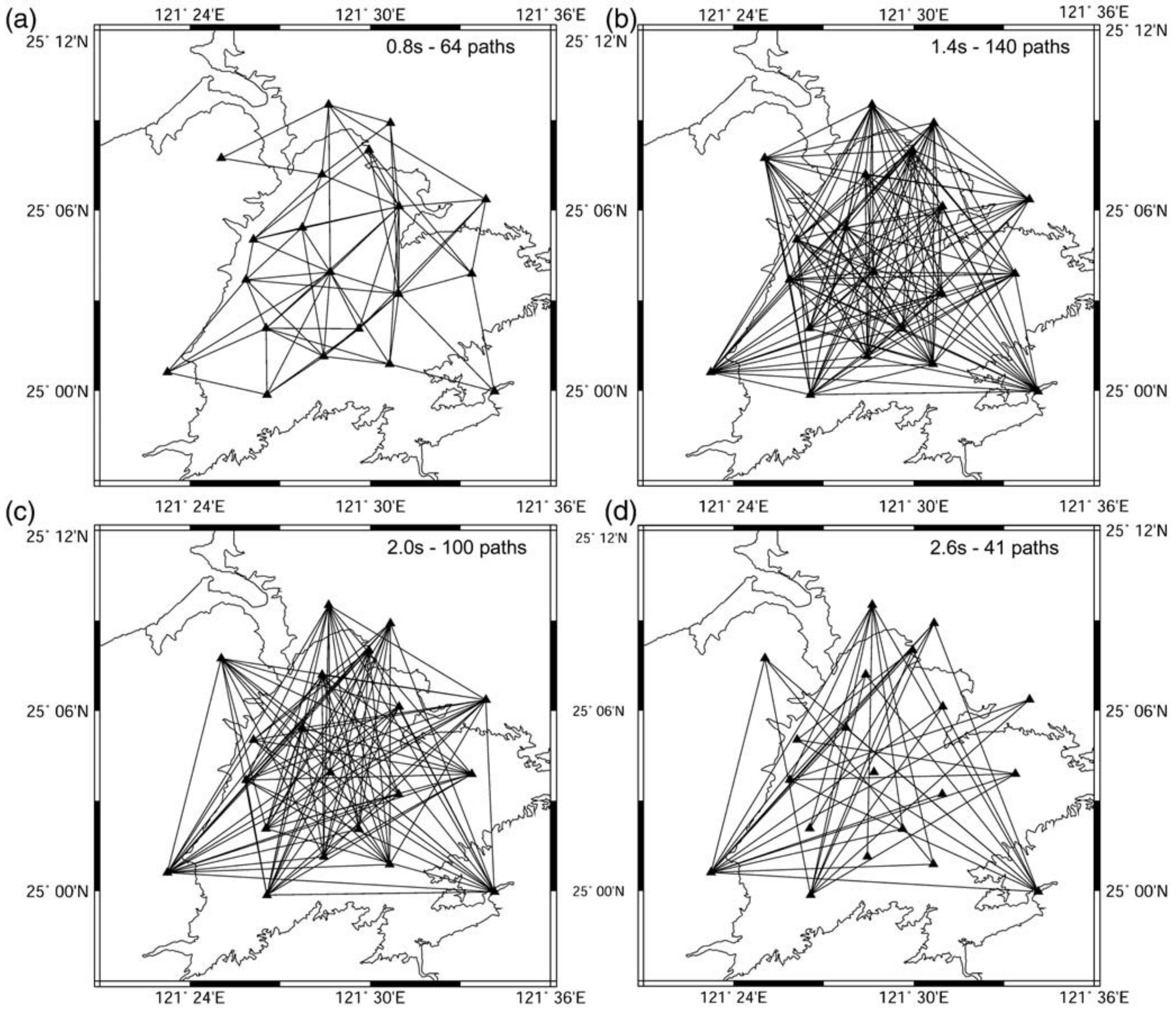

Figure 7. Path coverage of phase velocity measurements at four selected periods: (a) 0.8 s, (b) 1.4 s, (c) 2.0 s, and (d) 2.6 s.

Chung and Shin (1999) analyzed fundamental mode Love waves recorded at TSMIP after the 1994 Nanao earthquake (M_L 6.2). Using the frequency-wavenumber method, they estimated that Love-wave phase velocities are 1.3–1.75 km/s at periods of 2–3 s. This is the only previous surface wave study in the Taipei basin with which we can compare our results, but they had unknown timing errors that induced uncertainty in their wave speed estimates. In general, Love-wave phase velocities tend to be a few percent higher than Rayleigh-wave phase velocities (at the same periods and for the same continental structure). We found that the average Rayleigh-wave phase velocity of 1.5–1.7 km/s obtained in this study is similar to (within the range of standard deviation) their obtained Love-wave phase velocities (1.3–1.75 km/s) at 2–3 s. This implies general consistency between our study and the study by Chung and Shin (1999).

Path Coverage and Lateral Resolution

Figure 7 shows path coverage of phase velocity measurements at four selected periods in the Taipei basin. The path coverage at very short periods ($T = 0.5$–1.0 s) is poor (Fig. 7a), but the number of paths exceeds 100 at $T = 1.1$–2.0 s. There are 140 paths at $T = 1.4$ s (Fig. 7b), with very good coverage in the central part of the Taipei basin. The path number is less than 100 at $T > 2.1$ s and decreases to 41 at $T = 2.6$ s (Fig. 7d), but still with good path coverage. At periods longer than 2.7 s, the number of station pairs is only about 30 or less. Furthermore, there are no paths in the eastern and southern margins of the Taipei basin.

We use the generalized least-squares inversion method (Tarantola and Nercessian, 1984; Yao *et al.*, 2005) to invert for 2D variation of phase velocity at each period from the obtained dispersion measurements. A Gaussian correlation function is used in the inversion to stabilize the inversion and control the smoothness of the solution. The study region is parameterized by 0.02° × 0.02° grid points; there are 10 grid points in the north–south direction and 11 grid points in the east–west direction. Before inversion of the dispersion measurements for 2D phase velocity variation, we performed a checkerboard resolution test (CRT) to evaluate the lateral resolution of phase velocity map at each period. We note that the recovery of checkerboards depends primarily on path coverage and the accuracy of the inversion code and not on the (true) errors in the data. The input anomalies have a 0.05° length scale and a velocity contrast of 1.5 ± 0.2 km/s (Fig. 8). Figure 9 shows the recovery for the four selected periods with path coverage shown in Figure 7. At period 0.8 s, poor path coverage and low path density result in poor recovery (Fig. 9a). However, we can still resolve the checkerboard pattern in the center of the study region. At periods larger than 1.1 s (Fig. 9b,c,d), we can recover the input checkerboard model in most parts of the study region, except in the western margin and corners of the study area where slight smearing seems to occur. Overall, for the periods interested in this study, we can resolve anomalies as small as 5 km wavelength in most of our study region.

Phase Velocity Maps

For periods $T = 0.5$–3 s (with 0.1 s interval), we construct phase velocity maps with 0.02° grid spacing using a 2 km correlation length (smoothing factor). Figure 10 shows phase velocity maps at six periods. As a rule of thumb, Rayleigh-wave phase velocity is most sensitive to the shear-wave velocity structure at a depth around one-third wavelength. Therefore, the most sensitive depth increases from 200–500 m at $T = 0.8$ s to 1000–2000 m at $T = 2.6$ s (Fig. 10). At 0.8 s (Fig. 10a), low velocities appear in the western part of the Taipei basin, which is along the Chinshan fault and the Shanchiao fault and extends eastward from the Linkou tableland to Panchiao, Shulin, Yunghe, and Wanhua. High velocity is inferred in the eastern part of the Taipei basin and beneath Kuanyin Mountain. At $T = 1.2$ s (Fig. 10b), the low-velocity region is similar to that at $T = 0.8$ s, but it extends farther east toward Sungshan. Thus, a low-velocity area is also along the Taipei fault. There is also a local low-velocity area in Yuanshan. High velocities mark the southern part of the Tatun volcanic area, extend southward inside the basin, and terminate around the Kanchiao fault. Surrounding mountains such as the Kuanyin Mountain and the Western Foothills are also characterized by higher-than-average phase speeds. The high velocity area in the southern part of the Tatun volcanic area reaches southward to Wanhua at $T = 1.6$ s (Fig. 10c). At $T = 1.8$ s (Fig. 10d), the high velocity regions in the Tatun volcanic area and Kuanyin Mountain connect with each other in Kuantu Plain. The features are generally similar at $T = 2.2$ s and 2.6 s (Fig. 10e,f), with low phase speeds beneath the Linkou tableland and along the Chinshan fault, the Shanchiao fault, and the Taipei fault, whereas high velocities appear in the Tatun volcanic area, Kuanyin Mountain, the Western Foothills, and Wanhua.

The obtained phase velocity distribution agrees very well with surface geology. High phase velocity regions appear in the Tatun volcanic area and Kuanyin Mountain, which are dominated by Quaternary igneous rock, and to the south of Taipei fault, which belongs to Miocene Western Foothills. Another high velocity region is observed in the southern part of the Tatun volcanic area, east of Kuantu Plain, which extends southward and terminates around the Kanchiao fault from $T = 1.1$ s. For $T > 1.5$ s, the high velocity region extends southward to Wanhua, a shallow Tertiary basement in the middle of the Taipei basin (Wang and Sun, 1999). Low-velocity anomaly appears mainly in the Pleistocene Linkou tableland and along the western and southeastern edges of the Taipei basin. In Yuanshan, the phase velocity is also slow at $T = 1.2$–2.1 s, but there are no apparent geologic features at the surface corresponding to this low-velocity region.

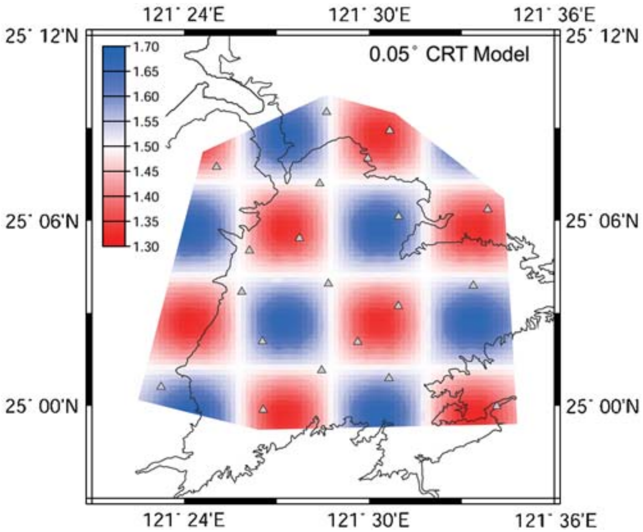

Figure 8. Input 0.05° × 0.05° checkerboard resolution test (CRT) model with velocity 1.5 ± 0.2 km/s in this study.

Discussion

Most previous ambient seismic noise tomography studies use data in the period range 10–30 s. The study presented here demonstrates that ambient seismic noise tomography is also feasible at much shorter periods ($T = 0.5$–3 s), provided that the interstation distance is also much shorter (about 5 km). For much larger interstation distance, it is difficult to recover short-period TDEGFs because of attenuation. In general, the spectral extent of ambient seismic noise tomography is limited by the interstation distance, while the lateral resolution is controlled by the geometry of the array. The shorter the interstation distance, the higher the frequency that ambient seismic noise tomography can use.

Our results reveal that faults may play an important role in the regional tectonics of the Taipei basin. The Chinshan fault and the Shanchiao fault are characterized by a low-velocity zone in the deepest part of the Tertiary basement; they divide the high velocity Quaternary igneous rock of the Tatun volcanic area and Kuanyin Mountain into two parts. The Taipei fault (along the southern border of the Taipei basin) marks the transition from the high-velocity Miocene Western Foothills to the south to the low-velocity Holocene sediments to the north. At $T = 1.1$–1.4 s, the Kanchiao fault, which has been considered as a terrane boundary (Wang *et al.*, 2004), truncates the high-velocity region from the southern part of Tatun volcanic area. Besides, the low-velocity zones that we infer from the phase velocity maps may represent damage zones in the Taipei basin. That is because low wave speed zones are easy to trap and amplify seismic energy when seismic waves transit. Using this concept, Prieto and Beroza (2008) tried to predict earthquake ground motion with ambient seismic noise field in the Los Angeles basin.

Ambient seismic noise, also called microseism or microtremor, is caused by human activities, atmospheric pressure changes, interaction of ocean waves with coast and seafloor, and so on. Some studies (Bromirski, 2001; Gerstoft, Fehler, and Sabra, 2006; Webb, 2007; Traer *et al.*, 2008) suggested that most ambient seismic noise sources generated by ocean waves are in the shallow water continental shelf rather than the deep open sea. Several studies (e.g., Stehly *et al.*, 2006; Yang and Ritzwoller, 2008; Yao and van der Hilst, 2009; Yao *et al.*, 2009) discussed the generation of ambient seismic noise sources in some detail. It is generally accepted that the secondary microseisms (in the period band 5–10 s) are

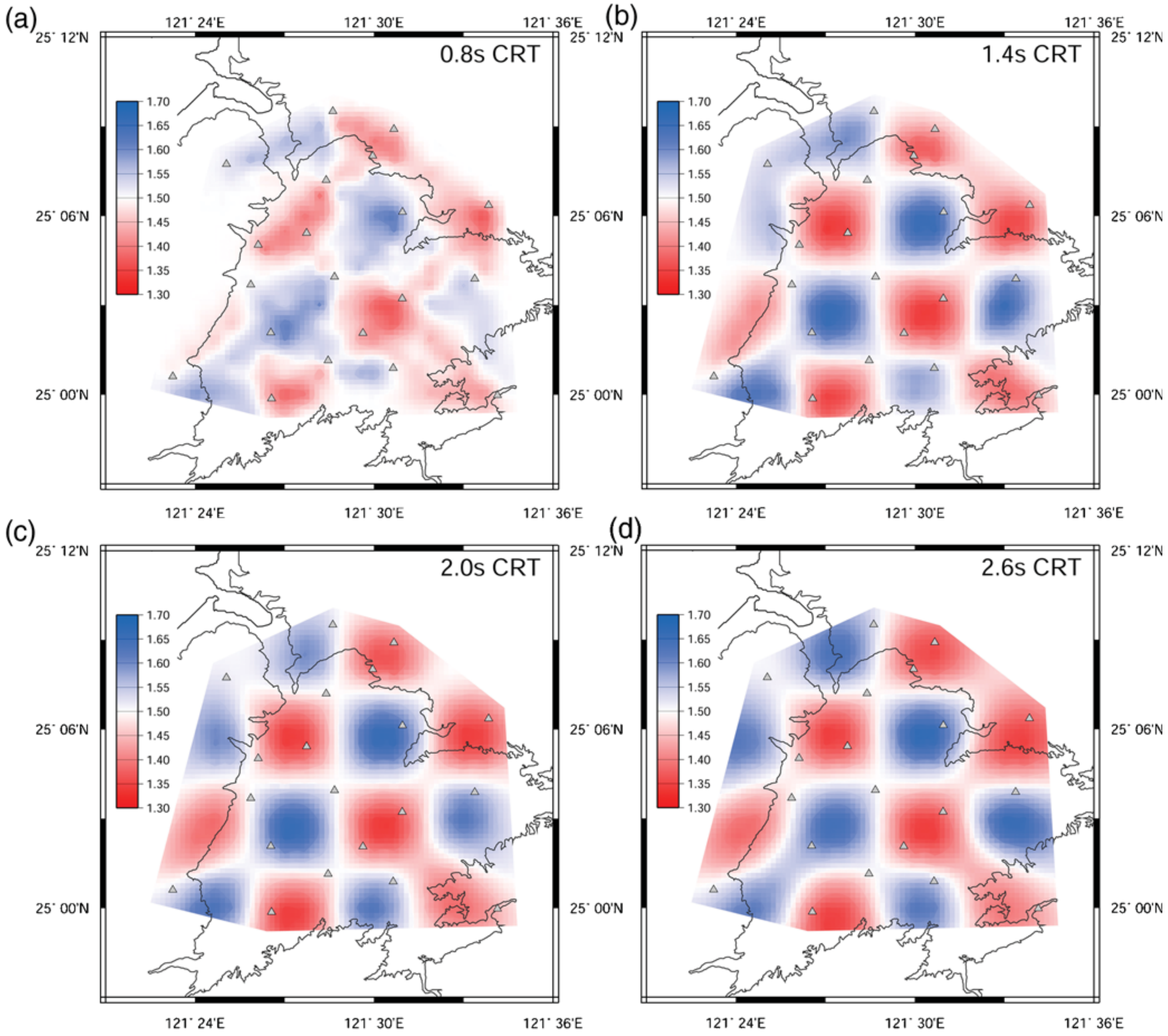

Figure 9. Recovery of 0.05° × 0.05° CRT model at the four periods with path coverage shown in Figure 7.

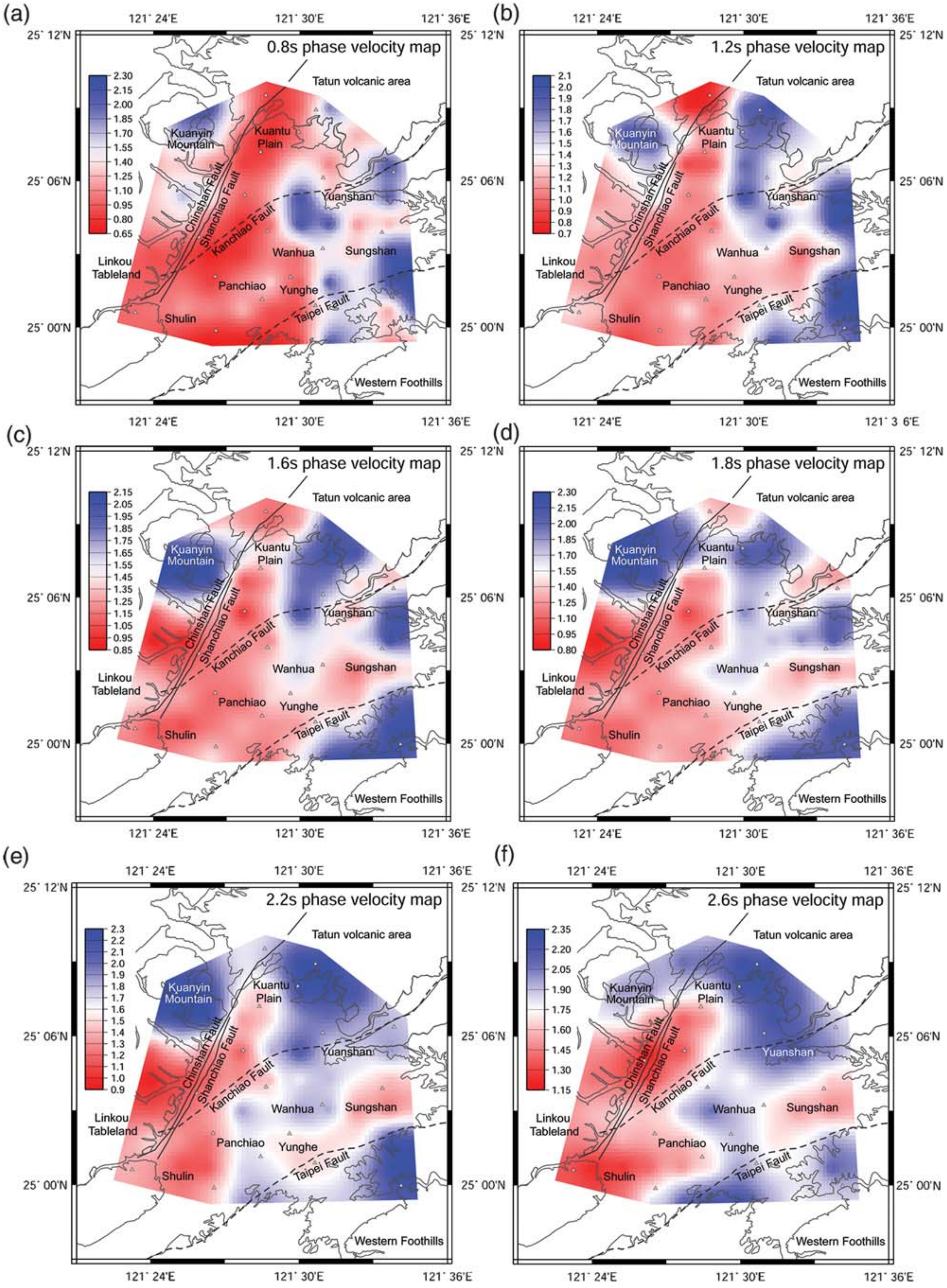

Figure 10. Phase velocity maps at six periods in the Taipei basin: (a) 0.8 s, (b) 1.2 s, (c) 1.6 s, (d) 1.8 s, (e) 2.2 s, and (f) 2.6 s.

mainly generated by ocean wave interactions with the seafloor near coastlines or shallow water. However, the generation of the primary microseisms (in the period band 10–20 s) is still debated, with some arguing for ocean wave activity in the deep sea (Stehly *et al.*, 2006), while others attribute it to the interaction between ocean waves and coastlines (Yang and Ritzwoller, 2008). Around the Island of Taiwan, the continental shelf is off the west coast of Taiwan (Taiwan Strait), whereas the seafloor gradient increases rapidly off the east coast of Taiwan (Pacific Ocean). Our analysis of azimuthal dependence of the normalized amplitudes of TDEGFs (Figs. 4b and 5) shows that ambient seismic noise sources at 0.5–5 s period band (close to the secondary microseism period band) are mainly northwest of the study region, and the coastlines and continental shelf of the Taiwan Strait are probable candidates.

Many of the world's largest metropolitan regions are in regions with relatively low regional seismicity; some may be located inside an alluvial basin, such as the Taipei basin. In these situations, 3D crustal heterogeneity cannot be determined effectively with traditional earthquake tomography and long-range seismic explosion experiments. However, shallow structure plays an important role in characterizing site effect and for constructing strong ground motion, which are very important for mitigating seismic hazards. We show here that surface wave array tomography with TDEGFs from ambient seismic noise can be used to characterize the shallow subsurface beneath a metropolitan region. The broadband seismic array used in this study was redeployed in a broader region around the Taipei basin one year later with more stations. In the future, we will combine data from this new array to invert for shear-wave velocity structure in the shallow crust (top several kilometers) in the Taipei basin and surrounding area.

Conclusions

We performed ambient seismic noise tomography at very short periods (0.5–3 s) in the Taipei basin with high ambient seismic noise level due to natural and human activity. From analysis of the azimuthal dependence of the normalized amplitudes of TDEGFs, we infer that dominant ambient seismic noise source (in the period band $T =$ 0.5–5 s) is toward the northwest of the study region, with the coastlines and shallow continental shelf in the Taiwan Strait likely candidates. Our ambient seismic noise tomography provides important information on the shallow crustal structure in the Taipei basin; the inferred lateral variations in phase velocity correlate well with surface geology in the region. For instance, high phase velocity regions characterize the Tatun volcanic area, Kuanyin Mountain (Quaternary igneous rock), and the Miocene Western Foothills south of Taipei fault. Low phase velocity regions mark the western and southeastern edges of the Taipei basin and Pleistocene Linkou tableland. The major faults in the Taipei basin are either characterized by low-velocity anomaly or mark the transition between regions with high and low Rayleigh-wave phase speeds. In the future, we will combine data from more stations in a broader region surrounding the Taipei basin and invert for 3D shallow crustal structure.

Data and Resources

The data used in this research were collected by the Institute of Earth Sciences, Academia Sinica and can be obtained through Bor-Shouh Huang. The programs for ambient seismic noise analysis and tomography were developed by Huajian Yao (MIT). Seismic Analysis Code (SAC) 2000 (www.iris.edu/manuals/sac/manual.html; Goldstein *et al.*, 2003) was used for data analysis. Some figures were made using the Generic Mapping Tools (GMT) version 3.3.2 (www.soest.hawaii.edu/gmt/; Wessel and Smith, 1998).

Acknowledgments

The authors would like to thank three anonymous reviewers and the editor who helped to improve the paper. Wen-Tzong Liang, Ban-Yuan Kuo, Li Zhao, Chih-Cheng Yang, Yu-Wen Chang, Che-Min Lin, Chung-Han Chan, Yi-Ru Chen, and Ya-Chuan Lai gave constructive suggestions and helpful reviews of the paper. This research was supported by the Institute of Earth Sciences, Academia Sinica, and Central Geological Survey under Grant Number 5226902000-05-93-02, and National Science Council under Grant Number 97-2119-M-001-010.

References

Bensen, G. D., M. H. Ritzwoller, and N. M. Shapiro (2008). Broadband ambient noise surface wave tomography across the United States, *J. Geophys. Res.* **113,** B05306, doi 10.1029/2007JB005248.

Bromirski, P. D. (2001). Vibrations from the "Perfect Storm", *Geochem., Geophys., Geosyst.* **2,** no. 7, 1030, doi 10.1029/2000GC000119.

Campillo, M., and A. Paul (2003). Long-range correlations in the diffuse seismic coda, *Science* **299,** 547–549, doi 10.1126/science.1078551.

Central Geological Survey (2000). An introduction to the active faults of Taiwan (second edition), *Central Geol. Surv. Spec. Pub.* **13,** MOEA, ROC, 121 pp. (in Chinese).

Chung, J. K., and T. C. Shin (1999). Surface-wave analysis in the Taipei basin from strong-motion data, *Terr. Atmos. Ocean. Sci.* **10,** 633–650.

Dahlen, F. A., and J. Tromp (1998) *Theoretical Global Seismology*, Princeton University Press, Princeton, New Jersey.

Gerstoft, P, M. C. Fehler, and K. G. Sabra (2006). When Katrina hit California, *Geophys. Res. Lett.* **33,** L17308, doi 10.1029/2006GL027270.

Gerstoft, P., K. G. Sabra, P. Roux, W. A. Kuperman, and M. C. Fehler (2006). Green's functions extraction and surface-wave tomography from microseisms in southern California, *Geophysics* **71,** S123–S131, doi 10.1190/1.2210607.

Goldstein, P., D. Dodge, M. Firpo, and L. Minner (2003). SAC2000: Signal processing and analysis tools for seismologists and engineers, invited contribution to *The IASPEI International Handbook of Earthquake and Engineering Seismology*, W. H. K. Lee, H. Kanamori, P. C. Jennings, and C. Kisslinger (Editors), Academic Press, London.

Kang, T. S., and J. S. Shin (2006). Surface-wave tomography from ambient seismic noise of accelerograph networks in southern Korea, *Geophys. Res. Lett.* **33,** L17303, doi 10.1029/2006GL027044.

Kim, K. H., J. M. Chiu, J. Pujol, K. C. Chen, B. S. Huang, Y. H. Yeh, and P. Shen (2005). Three-dimensional V_P and V_S structural models associated with the active subduction and collision tectonics in the Taiwan region, *Geophys. J. Int.* **162,** 204–220, doi 10.1111/j.1365-246X.2005.02657.x.

Larose, E., A. Derode, M. Campillo, and M. Fink (2004). Imaging from one-bit correlations of wideband diffuse wave fields, *J. Appl. Phys.* **95,** 8393–8399, doi 10.1063/1.1739529.

Lee, S. J., H. W. Chen, Q. Liu, D. Komatitsch, B. S. Huang, and J. Tromp (2008). Three-dimensional simulations of seismic-wave propagation in the Taipei basin with realistic topography based upon the Spectral-Element Method, *Bull. Seismol. Soc. Am.* **98,** 253–264, doi 10.1785/0120070033.

Lin, F. C., M. P. Moschetti, and M. H. Ritzwoller (2008). Surface wave tomography of the western United States from ambient seismic noise: Rayleigh and Love wave phase velocity maps, *Geophys. J. Int.* **173,** 281–298, doi 10.1111/j.1365-246X.2008.03720.x.

Lin, F. C., M. H. Ritzwoller, J. Townend, S. Bannister, and M. K. Savage (2007). Ambient noise Rayleigh wave tomography of New Zealand, *Geophys. J. Int.* **170,** 649–666, doi 10.1111/j.1365-246X.2007.03414.x.

Prieto, G. A., and G. C. Beroza(2008). Earthquake ground motion prediction using the ambient seismic field, *Geophys. Res. Lett.* **35,** L14304, doi 10.1029/2008GL034428.

Roux, P., K. G. Sabra, W. A. Kuperman, and A. Roux (2005). Ambient noise cross correlation in free space: Theoretical approach, *J. Acoust. Soc. Am.* **117,** 79–84.

Sabra, K. G., P. Gerstoft, P. Roux, W. A. Kuperman, and M. C. Fehler (2005a). Extracting time-domain Green's function estimates from ambient seismic noise, *Geophys. Res. Lett.* **32,** L03310, doi 10.1029/2004GL021862.

Sabra, K. G., P. Gerstoft, P. Roux, W. A. Kuperman, and M. C. Fehler (2005b). Surface wave tomography from microseisms in Southern California, *Geophys. Res. Lett.* **32,** L14311, doi 10.1029/2005GL023155

Shapiro, N. M., and M. Campillo (2004). Emergence of broadband Rayleigh waves from correlations of the ambient seismic noise, *Geophys. Res. Lett.* **31,** L07614, doi 10.1029/2004GL019491.

Shapiro, N. M., M. Campillo, L. Stehly, and M. H. Ritzwoller (2005). High-resolution surface-wave tomography from ambient seismic noise, *Science* **307,** 1615–1618, doi 10.1126/science.1108339.

Shapiro, N. M., M. H. Ritzwoller, and G. D. Bensen (2006). Source location of the 26 sec microseism from cross-correlations of ambient seismic noise, *Geophys. Res. Lett.* **33,** L18310, doi 10.1029/2006GL027010.

Stehly, L., M. Campillo, and N. M. Shapiro (2006). A study of the seismic noise from its long-range correlation properties, *J. Geophys. Res.* **111,** B10306, doi 10.1029/2005JB004237.

Tarantola, A., and A. Nercessian (1984). Three-dimensional inversion without blocks, *Geophys. J. R. Astr. Soc.* **76,** 299–306.

Teng, L. S., C. T. Lee, C. H. Peng, W. F. Chen, and C. J. Chu (2001). Origin and geological evolution of the Taipei basin, northern Taiwan, *Western. Pac. Earth Sci.* **1,** 115–142.

Traer, J., P. Gerstoft, P. D. Bromirski, W. S. Hodgkiss, and L. A. Brooks (2008). Shallow-water seismoacoustic noise generated by tropical storms Ernesto and Florence, *J. Acoust. Soc. Am.* **124,** EL170–EL176, doi 10.1121/1.2968296.

Wang, C. Y., and C. T. Sun (1999). Interpretation of seismic stratigraphy in the Taipei basin, *Central Geol. Surv. Spec. Pub.* **11,** MOEA, ROC, 273–292 (in Chinese).

Wang, C. Y., Y. H. Lee, M. L. Ger, and Y. L. Chen (2004). Investigating subsurface structures and *P*- and *S*-wave velocities in the Taipei basin, *Terr. Atmos. Ocean. Sci.* **15,** 609–627.

Webb, S. C. (2007). The Earth's 'hum' is driven by ocean waves over the continental shelves, *Nature* **445,** 754–756, doi 10.1038/nature05536.

Wen, K. L., and H. Y. Peng (1998). Site effect analysis in the Taipei basin: Results from TSMIP network data, *Terr. Atmos. Ocean. Sci.* **9,** 691–704.

Wessel, P., and W. H. F. Smith (1998). New, improved version of the generic mapping tools released *Eos Trans. AGU* **79,** 579.

Yang, Y., and M. H. Ritzwoller (2008). Characteristics of ambient seismic noise as a source for surface wave tomography, *Geochem., Geophys., Geosyst.* **9,** Q02008, doi 10.1029/2007GC001814.

Yang, Y., M. H. Ritzwoller, A. L. Levshin, and N. M. Shapiro (2007). Ambient noise Rayleigh wave tomography across Europe, *Geophys. J. Int.* **168,** 259–274, doi 10.1111/j.1365-246X.2006.03203.x.

Yao, H., and R. D. van der Hilst (2009). Analysis of ambient noise energy distribution and phase velocity bias in ambient noise tomography, with application to SE Tibet, *Geophys. J. Int.* **179,** 1113–1132, doi 10.1111/j.1365-246X.2009.04329.x.

Yao, H., C. Beghein, and R. D. van der Hilst (2008). Surface wave array tomography in SE Tibet from ambient seismic noise and two-station analysis—II. Crustal and upper-mantle structure, *Geophys. J. Int.* **173,** 205–219, doi 10.1111/j.1365-246X.2007.03696.x.

Yao, H., X. Campman, M. V. de Hoop, and R. D. van der Hilst (2009). Estimation of surface wave Green's functions from correlation of direct waves, coda waves, and ambient noise in SE Tibet, *Phys. Earth Planet. In.* **177,** 1–11, doi 10.1016/j.pepi.2009.07.002.

Yao, H., R. D. van der Hilst, and M. V. de Hoop (2006). Surface-wave array tomography in SE Tibet from ambient seismic noise and two-station analysis—I. Phase velocity maps, *Geophys. J. Int.* **166,** 732–744, doi 10.1111/j.1365-246X.2006.03028.x.

Yao, H., G. Xu, L. Zhu, and X. Xiao (2005). Mantle structure from interstation Rayleigh wave dispersion and its tectonic implication in western China and neighboring regions, *Phys. Earth Planet. Inter.* **148,** 39–54, doi 10.1016/j.pepi.2004.08.006.

Institute of Geophysics
National Central University
300 Jhongda Road, Jhongli City
Taoyuan County 32001, Taiwan
nativemanncu@gmail.com
wenkl@earth.ncu.edu.tw
(Y.-C.H., K.-L.W.)

Department of Earth, Atmospheric, and Planetary Sciences
Massachusetts Institute of Technology
77 Massachusetts Avenue
Cambridge, Massachusetts 02139
hjyao@mit.edu
hilst@mit.edu
(H.Y., R.D.v.)

Institute of Earth Sciences
Academia Sinica
128 Academia Road, Section 2
Nankang, Taipei 11529, Taiwan
hwbs@earth.sinica.edu.tw
wgee@earth.sinica.edu.tw
(B.-S.H., W.-G.H.)

Central Geological Survey
Ministry of Economic Affairs
2, Lane 109, Huasin Street, Jhonghe City
Taipei County 23568, Taiwan
prochen@moeacgs.gov.tw
(C.-H.C.)

Manuscript received 1 October 2009